J Mater Sci (2026) 61:32656–32672

Ceramics

Entropy-assisted stabilization of cubic bixbyite phases in multicomponent rare-earth oxides

Antonio de Nigris[1], Luca Spiridigliozzi[2,3,4,5], Ginfranco Dell'Agli[5], and Luigi Ambrosone[1,*]

[1] *Department of Medicine and Health Sciences, "V. Tiberio", University of Molise, Via De Sanctis, 86100 Campobasso, Italy*
[2] *Department of Engineering and Science, Universitas Mercatorum, Piazza Mattei 10, 00186 Roma, Italy*
[3] *INSTM, National Interuniversity Consortium of Materials Science and Technology, Via G. Giusti 9, 50121 Florence, Italy*
[4] *EUT, Institute of Nanomaterials and Nanotechnologies-EUTINN, European University of Technology, 03043 Cassino, FR, Italy*
[5] *Department of Civil and Mechanical Engineering, University of Cassino and Southern Lazio, Via G. di Biasio 43, 03043 Cassino, FR, Italy*

Received: 13 April 2026
Accepted: 6 September 2026
Published online: 17 September 2026

© The Author(s), 2026

ABSTRACT

Rare-earth oxides provide a model platform for examining how configurational entropy reshapes the interplay between crystal structure, lattice dynamics, and redox chemistry. Here, we compare single-component Ln_2O_3 sesquioxides (Ln = Gd, Dy, Y, Yb, Lu) with two equimolar high-entropy oxides (HEO-Lu and HEO-Tb) designed to differ only in the identity of a single cation. While the reference sesquioxides adopt the cubic bixbyite structure and exhibit smooth thermal and optical responses, terbium oxide behaves fundamentally differently: The electronic accessibility of the $Tb^{3+} \leftrightarrow Tb^{4+}$ redox couple stabilizes oxygen-rich, mixed-valence phases with triclinic symmetry and localized electronic states. Under nitrogen, however, terbium remains fully trivalent, and both high-entropy oxides form single-phase cubic solid solutions with no evidence of symmetry lowering, oxygen release, or redox transitions. Laboratory XRD and synchrotron total-scattering measurements confirm that the cubic framework is preserved at both the average and local scale, demonstrating that configurational entropy contributes to hinder the structural instabilities intrinsic to terbium oxide. Notably, HEO-Tb accommodates terbium in a chemically flexible environment capable of hosting excess oxygen without triggering local distortions, revealing an oxygen-buffering behavior that is inaccessible in the binary oxide. Calorimetric measurements show positive deviations from ideal mixing in the molar heat capacity, consistent with phonon broadening and enhanced low-frequency vibrational activity induced by chemical disorder. Optical absorption spectra further support this entropy-assisted homogenization: Both HEO-Lu and HEO-Tb exhibit widened band gaps relative to their single-component analogs, reflecting the suppression

Communicated by Julia Glaum.

Address correspondence to E-mail: ambroson@unimol.it
E-mail Addresses: a.denigris1@studenti.unimol.it; l.spiridigliozzi@unicas.it; dellagli@unicas.it

https://doi.org/10.1007/s10853-026-13752-2

of defect-related absorption tails and the elimination of localized states associated with mixed valence in terbium oxide. Overall, our results demonstrate that multicationic cubic structures can be synthesized even when incorporating chemically complex or intrinsically unstable constituents, yielding rare-earth oxides with homogenized vibrational, electronic, and redox landscapes. These findings highlight high-entropy design as a robust strategy for engineering oxide materials with enhanced structural stability, tunable phonon spectra, and chemically flexible oxygen-handling capabilities.

Introduction

The development of ceramic materials that combine high thermal stability, defect tolerance, and multifunctional behavior remains a central challenge in advanced materials science [1, 2]. High-entropy oxides (HEOs) have emerged as a promising class of materials in which configurational entropy stabilizes single-phase solid solutions composed of multiple equimolar cations sharing a common crystallographic site [3, 4]. In these systems, the entropic contribution lowers the Gibbs free energy, enabling homogeneous phases even among constituents that would normally segregate or adopt distinct crystal structures. For an equimolar five-cation composition, the ideal configurational entropy is fixed at $\Delta S_{config} = R \ln 5$ per mole of cations, independently of the identities of the five species. Such value is sufficient to define equimolar multicationic systems as high-entropy oxides (HEOs), even if a fully reversible entropy-driven transition from a single-phase to a multiphasic system at a fixed temperature is necessary to define them as entropy-stabilized oxides (ESOs) [5, 6]. Consequently, the configurational entropy contribution alone can favor statistical cation mixing and oppose segregation, but it cannot by itself explain *a priori* why a specific rare-earth-based multicationic system adopts the bixbyite rather than the fluorite or a multiphase structure. Early studies on multicomponent rare-earth oxides demonstrated that extensive mixing across the lanthanide series can yield stable cubic bixbyite phases despite large variations in ionic radius and coordination preferences [7]. These results established the conceptual basis for entropy-driven stabilization in rare-earth systems. More recent computational work has shown that exchange-correlation approximations in density functional theory struggle to capture the interplay between valence stability, oxygen stoichiometry, and lattice distortion in rare-earth oxides [8], underscoring the need for experimental benchmarks capable of disentangling disorder, redox activity, and structural stabilization. Rare-earth-based high-entropy oxides (RE-HEOs) are particularly appealing because subtle variations in ionic radius, valence stability, and crystal-field effects across the lanthanide series allow fine control over lattice distortion, defect chemistry, and oxygen-vacancy concentration. These structural features underpin the thermal robustness and functional versatility of RE-HEOs, which exhibit tunable optical [9], electrical [10], and mechanical properties [11, 12]. As a result, RE-HEOs are attracting increasing interest for applications in high-temperature coatings, optical ceramics, catalytic supports, and energy-conversion devices. In contrast, individual rare-earth sesquioxides are well known for their refractory nature, low thermal expansion, and distinctive optical and magnetic characteristics [13]. However, their physical properties are constrained by limited compositional degrees of freedom, which restrict the tunability of lattice dynamics, thermodynamic response, and defect landscape. For this reason, the sesquioxides Ln_2O_3 (Ln = Gd, Dy, Y, Yb, Lu) serve as essential reference systems: their well-defined cubic bixbyite structure and stable stoichiometry provide a baseline against which the effects of configurational disorder in HEOs can be quantitatively assessed. Establishing this baseline is crucial for determining whether the emergent behavior of RE-HEOs arises from entropy-driven homogenization or from the intrinsic chemistry of the constituent lanthanides. Recent spectroscopic and scattering studies have begun addressing this question directly. Lanthanide L-edge spectroscopy revealed that valence fluctuations and local coordination environments in HEOs remain sensitive to the degree of disorder, providing insight into redox behavior and phase stability in multicomponent systems [14]. Complementary work has shown that structural transitions in lanthanide HEOs can be resolved through advanced diffraction and total-scattering techniques, demonstrating how disorder suppresses symmetry lowering and stabilizes

average cubic frameworks even in the presence of strongly anisotropic constituents [15]. Together, these studies highlight the need to test the robustness of entropy-driven stabilization against chemically complex and intrinsically unstable rare-earth elements. In this context, terbium represents a particularly revealing choice [13]. Unlike lutetium, terbium exhibits mixed valence, strong redox activity, and a marked tendency toward low-symmetry oxide structures. These features introduce competing energetic contributions that are absent in more chemically compliant rare-earth oxides. Substituting Lu with Tb therefore provides an opportunity to probe whether configurational entropy can help stabilize a simple average structure even when one of the constituent elements intrinsically favors structural complexity, oxygen nonstoichiometry, and localized electronic states. Previous investigations have demonstrated extensive cation mixing in rare-earth oxides, identified cation-specific effects on optical and valence properties, and mapped composition- and temperature-dependent transitions between bixbyite, fluorite and vacancy-ordered structures. The distinctive contribution of the present work is a direct, experimentally grounded comparison between two high-entropy oxides, HEO-Lu and HEO-Tb, designed to differ only in the identity of a single cation. To interpret their behavior, we complement the multicomponent analysis with a systematic characterization of the corresponding sesquioxides Ln_2O_3 and of the structurally complex Tb11O20. Unlike previous studies that focused on chemically simple lanthanides [7] or on spectroscopic signatures of disorder [14], our approach integrates structural characterization (XRD and synchrotron total scattering) with detailed thermal and thermodynamic analyses (TGA, DSC, and heat capacity). This combined methodology allows us to elucidate how chemically induced frustration influences lattice stability, vibrational behavior, and entropy-driven phase formation in rare-earth oxide solid solutions. Finally, the inclusion of terbium provides an opportunity to examine whether the compositionally complex lattice can accommodate oxygen-rich coordination environments without triggering mixed-valence transitions or structural distortions. This aspect, while not previously emphasized in the literature, is central to understanding how configurational disorder modulates redox flexibility and oxygen-handling capability in chemically complex oxides.

Experimental

Materials

Rare-earth nitrates $RE(NO_3)_3$ (RE = Dy, Y, Yb, Gd, Tb, Lu), ammonium carbonate (NH4)2CO3, and rare-earth sesquioxides RE_2O_3 (RE = Dy, Y, Yb, Gd, Tb, Lu) were purchased from Sigma-Aldrich and used without further purification. Prior to synthesis, all sesquioxides were calcined at 800 °C for 2 h in static air to remove adsorbed species and ensure stoichiometric oxygen content. Two multicomponent high-entropy oxides with nominal composition

$$(Dy_{0.2}Y_{0.2}Gd_{0.2}Yb_{0.2}X_{0.2})_2O_3$$

where X = Tb or Lu, were synthesized following a coprecipitation route adapted from Ref. [16]. This method ensures homogeneous cation mixing at the molecular scale, a prerequisite for entropy-driven stabilization during calcination. Aqueous solutions of the rare-earth nitrates were prepared to obtain a total cation concentration of 0.1 M (0.02 M for each cation). This precursor solution (solution A) was vigorously stirred to ensure complete dissolution. In parallel, a precipitating solution (solution B) was prepared by dissolving ammonium carbonate in deionized water to achieve a carbonate-to-cation molar ratio of $R = 10$, promoting rapid and complete precipitation of mixed rare-earth carbonates. Solution B was rapidly poured into solution A under mild stirring, resulting in the immediate formation of a homogeneous pinkish precipitate. The suspension was vacuum-filtered, thoroughly washed with deionized water to remove residual nitrates and ammonium ions, and dried overnight at 80 °C. The as-prepared powders were then calcined at 800 °C to induce crystallization and promote configurational entropy stabilization [17]. The resulting materials are hereafter referred to as HEO-Lu and HEO-Tb.

Methods

Thermogravimetric analysis (TGA)

Thermogravimetric measurements were performed using a Mettler Toledo TGA 2 (Switzerland). Approximately 5–10 mg of samples were placed in an alumina crucible and heated from 25 to 1000 °C under a dry nitrogen flow (80 cm^3 min^{-1}). A heating rate of 10 °

C min^{-1} was used for all experiments. TGA data were analyzed to assess mass stability, oxygen release, and redox behavior.

Differential scanning calorimetry (DSC)

Differential scanning calorimetry was carried out using a Mettler Toledo DSC 5+ instrument. Samples (5–10 mg) were sealed in standard aluminum crucibles, with an empty crucible serving as reference. Measurements were performed under dry nitrogen flow (80 cm^3 min^{-1}) using a heating rate of 10 °C min^{-1} over the temperature range 25–600 °C. Instrument baseline scans were performed using empty crucibles. DSC traces were analyzed to identify phase transitions, redox events, and thermodynamic anomalies.

Optical absorption spectroscopy

UV–Vis absorption spectra were recorded using a Cary 100 (Varian) spectrophotometer equipped with thermostatted quartz cuvettes. Approximately 5 mg of powder were dispersed in ultrapure water and vortexed for 1 min to ensure homogeneous suspension. Spectra were collected at room temperature in the 200–800 nm wavelength range. Band-gap energies were estimated using the Kubelka–Munk formalism.

X-ray diffraction (XRD)

Powder X-ray diffraction patterns were collected using a PANalytical X'Pert MPD diffractometer equipped with a Cu Kα radiation source ($\lambda = 1.5406$ Å). XRD data were used to determine phase purity, lattice parameters, and microstructural features such as crystallite size and microstrain.

Synchrotron powder X-ray diffraction (XRD)

Total-scattering measurements [18, 19] were performed at beamline ID31 (ESRF). Powders were loaded in ~1-mm cylindrical Kapton-sealed wells using a high-throughput holder. The HEO-Tb sample was measured in transmission geometry at 75.051 keV ($\lambda = 0.16520$ Å). Data were collected with a Pilatus CdTe 2 M detector (1679×1475 pixels, 172×172 μm^2) positioned with the direct beam in the detector corner; the sample-detector distance was ~0.3 m. Empty-well measurements were summed to generate the background. Geometry calibration used NIST SRM 660b (LaB_6). Azimuthal integration was performed with `pyFAI`, applying flat-field, geometry, solid-angle, and polarization corrections; invalid pixels and azimuthal outliers were masked via sigma-clipping. Backgrounds were scaled to each dataset and subtracted. Rietveld refinements were carried out in `TOPAS` v7 [20], fixing the LaB_6 lattice parameter to extract the instrumental profile and correct offset effects including parallax [21]. The PDFs were first generated automatically using `PDFgetX3` [22–24] over multiple Q_{max} values and then reprocessed using a Lorch modification function [25] to suppress termination ripples and high-frequency noise. Small-angle scattering was extrapolated from $Q_{min} \approx 0.3$ $Å^{-1}$ to 0. In the $G(r)$ curves, the gray-shaded region marks the unreliable low-r range associated with the r_{poly} parameter in `PDFgetX3`.

Thermal stability tests

To assess whether the cubic bixbyite phase(s) could represent a transient product kinetically trapped after synthesis, the Tb-containing multicomponent oxide was subjected to different additional thermal cycles. The as-precipitated precursor was calcined directly at 800 °C for 2 h and at 1500 °C for 1 h. In addition, powder previously calcined at 800 °C for 1 h was further annealed at 800 °C for 16 h or at 1500 °C for 16 h. Powder X-ray diffraction was collected after each treatment to determine whether prolonged annealing or increased temperature promoted phase separation or symmetry changes. The spatial distribution of Dy, Y, Gd, Yb, Tb and O on samples treated at 1500 °C for 1 and 16 h was investigated by scanning electron microscopy coupled with energy-dispersive X-ray spectroscopy. Elemental maps were acquired from representative regions to assess micrometer-scale compositional homogeneity and identify any Tb-rich or cation-depleted domains. X-ray photoelectron spectra (XPS) were collected using an Axis DLD Ultra photoelectron instrument (Kratos-Manchester UK). Charge compensation was needed for data acquisition. Flood gun conditions were optimized by maximizing the peak intensity and minimizing the peak at the full width at half maximum of the main core line peaks.

Binding energy alignments of the spectra were done selecting the C1 s graphitic component at 286.6 eV.

Results and discussion

Thermal analysis

All single-component Ln_2O_3 oxides (Ln = Gd, Dy, Y, Yb, Lu), shown in Fig. 1a, exhibit essentially constant mass over the entire investigated temperature range. The total mass variation remains within experimental uncertainty, confirming the high thermal stability and fixed stoichiometry of these cubic bixbyite phases.

The corresponding DSC traces in Fig. 1b are featureless, with no detectable endothermic or exothermic events, indicating the absence of phase transitions, redox processes, or oxygen-sublattice rearrangements. This behavior is consistent with the rigid trivalent chemistry and structural simplicity of these rare-earth sesquioxides. In sharp contrast with the other rare-earth oxides, as shown in Fig. 1a, terbium oxide exhibits two distinct mass-loss events, the first, of about 1% around 700 K, and the second, amounting to 1.9% at 950 K. This peculiar thermal behavior originates from the non-stoichiometric chemistry of terbium oxides. When Tb_2O_3 is calcined at 800 °C for 2 h in air, it oxidizes to Tb_4O_7 according to the reaction [26, 27]:

$$2Tb_2O_3 + \tfrac{1}{2}O_2 \rightarrow Tb_4O_7 \quad (1)$$

During cooling, however, oxygen diffusion is extremely slow, and the system becomes kinetically trapped in the Tb_7O_12 structure [26, 27]. Upon exposure to air, this phase gradually reabsorbs oxygen and evolves toward $Tb_{11}O_{20}$, which is the thermodynamically stable form at room temperature. Consequently, although the initial precursor was Tb_2O_3, the material entering the thermal analysis is effectively $Tb_{11}O_{20}$. Under an inert N_2 atmosphere, where the partial pressure of O_2 is essentially zero, $Tb_{11}O_{20}$ undergoes a two-step reduction, occurring at markedly lower temperatures than in air. The first mass-loss event, observed at 700 K, corresponds to the reaction

$$Tb_{11}O_{20} \rightarrow \tfrac{11}{7}Tb_7O_{12} + \tfrac{4}{7}O_2 \quad (2)$$

with a theoretical mass loss of 0.88%, in agreement with the experimental value of 1.0%. The second reduction step, detected at 950 K, involves the further reduction of Tb_7O_12 to Tb_2O_3:

$$Tb_7O_{12} \rightarrow \tfrac{7}{2}Tb_2O_3 + \tfrac{1}{2}O_2 \quad (3)$$

yielding an expected mass loss of 1.90%, fully consistent with the measured value of 1.9%. The cumulative mass loss (2.9%) matches the sum of the two theoretical contributions (2.78%), confirming the sequential

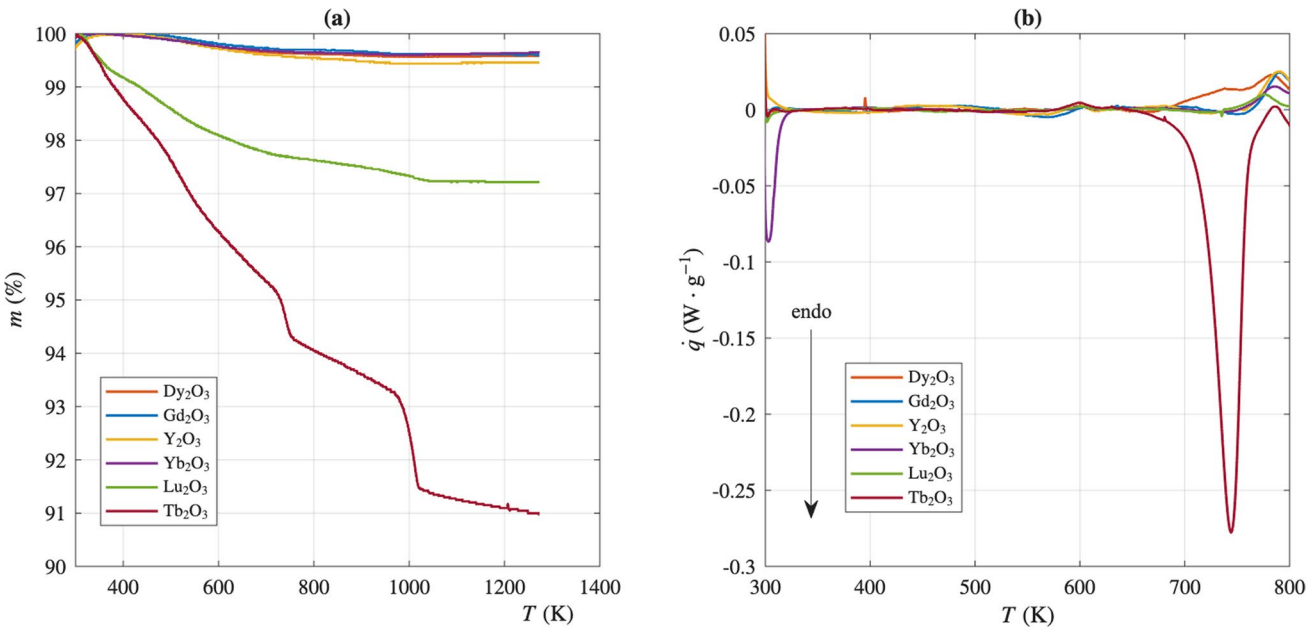


Figure 1 Calorimetric analysis of the single oxides. **a** TGA curves and **b** DSC curves.

reduction pathway Tb_11O_20 -> Tb_7O_12 -> Tb_2O_3. Figure 2a,b reports the thermal response of HEO–Tb and HEO–Lu. As shown in Fig. 2a, the TGA profile of HEO–Lu is smooth and continuous, showing no discrete mass-loss events or signatures of phase transitions. In contrast, HEO–Tb exhibits a measurable mass drop of 0.94% around 700 K. The gradual mass decrease observed in both materials is attributed to the release of surface species and/or the progressive formation of oxygen vacancies. The energy required for these processes is weak and absorbed continuously, resulting in a smooth calorimetric baseline. From Fig. 2a, the total mass loss for HEO-Lu is 5%, while for HEO-Tb it is 3.8%; if we subtract the 0.94% contribution from the peak at 700 K, the contribution from volatiles alone becomes 2.86%. Lu is the element that undergoes the greatest lanthanide contraction due to the contraction of the Lu^{3+} ionic radius, and this influences the concentration and stability of surface defects, resulting in a greater quantity of volatile species released during heating.

To investigate the nature of the mass loss (0.94%) observed at 700 K for HEO-Tb, let us reason as follows. The ideal structure of HEO–Tb is bixbyite-type $(Dy_{0.2}Gd_{0.2}Y_{0.2}Yb_{0.2}Tb_{0.2})_2O_3$, with all cations in the +3 oxidation state (symbolically M_2O_3), and that during synthesis in air all terbium is oxidized to +4 (symbolically $M_2O_{3.2}$), the thermal reduction under N_2 proceeds as

$$M_2O_{3.2} \rightarrow M_2O_3 + 0.1O_2 \quad (4)$$

This reaction predicts a theoretical mass loss of 0.92%, in excellent agreement with the experimental value of 0.94%. Therefore, the data are consistent with a structure in which terbium is oxidized to Tb^{4+} during synthesis.

Figure 2b shows the DSC profiles of both HEOs. HEO-Lu displays no significant features, only small oscillations attributable to instrumental noise. In contrast, HEO-Tb exhibits two endothermic peaks.

Molar heat capacity

Figure 3a displays the molar heat capacities $c_p(T)$ of the five reference sesquioxides Ln_2O_3 (Ln = Dy, Gd, Y, Yb, Lu). Although the large peak exhibited by Tb_2O_3 around 750 K dominates the full-scale plot, an expanded view of the 350–650 K region reveals that all oxides follow a common phononic trend [28, 29]. In this temperature window, the curves display smooth and monotonic increases consistent with the expected lattice contribution to the heat capacity, and each dataset is accurately reproduced by a standard Shomate fit [30]. The only deviation from smoothness is the mild oscillatory behavior of terbium oxide, yet even in this case the underlying progression remains compatible with a phonon-driven response. This shared behavior across the sesquioxides indicates that, despite differences in mass and local force constants, their lattice dynamics

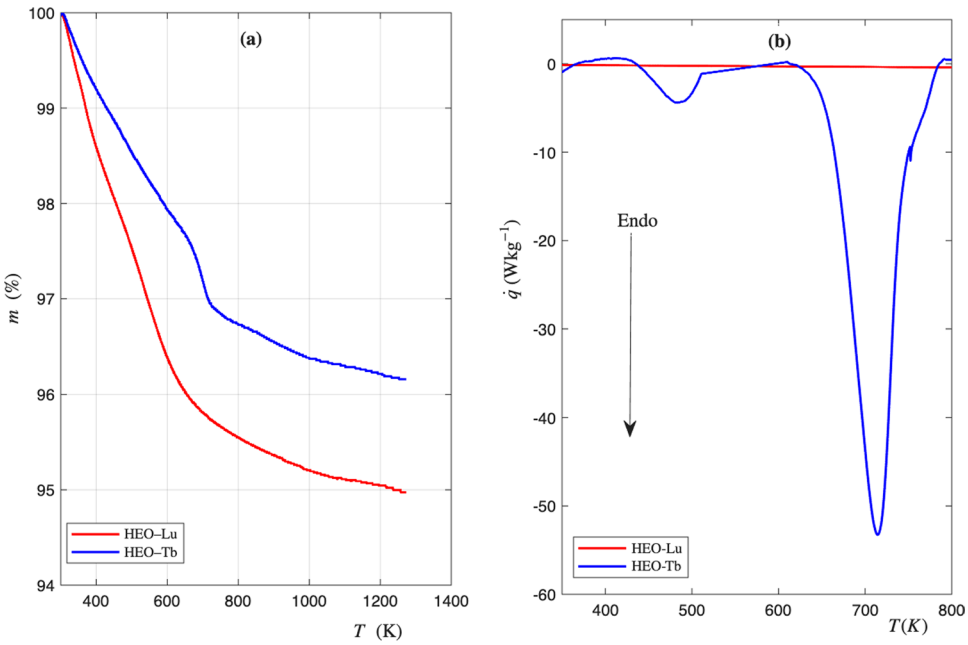


Figure 2 Calorimetric analysis of the HEOs. **a** TGA curves of HEO-Tb (blue) and HEO-Lu (red) **b** DSC curves of HEO-Tb (blue) and HEO-Lu (red).

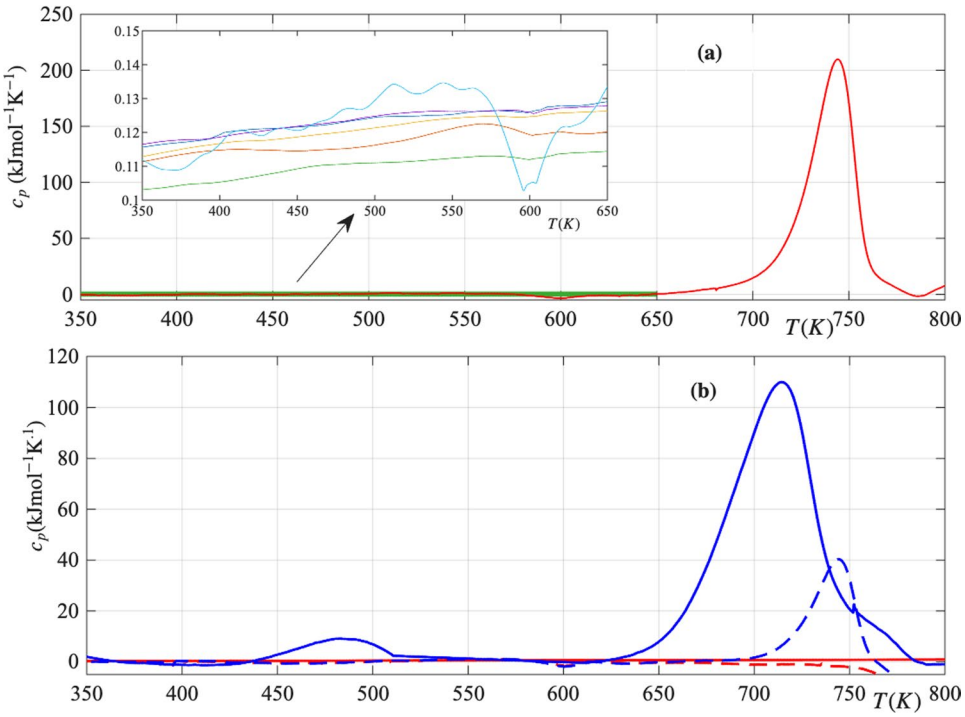


Figure 3 Molar heat capacities $c_p(T)$ of the rare-earth sesquioxides and the corresponding high-entropy oxides. **a** Heat-capacity curves of the single oxides Dy_2O_3, Gd_2O_3, Y_2O_3, Yb_2O_3, Lu_2O_3, and Tb_2O_3. The dominant peak of Tb_2O_3 near 750 K compresses the full-scale view, while the inset highlights the 350–650 K region where all oxides follow a common phononic trend. **b** Heat capacities of HEO-Lu (red) and HEO-Tb (blue), compared with their molar averages (dashed). HEO-Lu closely matches the average, whereas HEO-Tb shows a systematically higher $c_p(T)$ with two features: a shallow peak around 450–510 K and a broader one between 700 and 760 K, both attributable to lattice-dynamical contributions enhanced by configurational disorder.

in the intermediate-temperature regime are governed by comparable vibrational mechanisms. Figure 3b shows the corresponding heat capacities of the two high-entropy oxides. The HEO-Lu composition (red curve) closely follows the molar average of its constituent sesquioxides, with only minor deviations at higher temperatures. In contrast, the HEO-Tb system (blue curve) displays a systematically enhanced $c_p(T)$ over the entire temperature range. The molar-average curve (dashed line) shifts upward at elevated temperatures, yet remains consistently below the experimental data, demonstrating that the heat capacity of HEO-Tb cannot be described as a simple weighted combination of the pure oxides. Two distinct features emerge in the HEO-Tb curve. The first is a shallow peak of approximately 10 kJ mol^{-1} K^{-1} with a base width spanning 450–510 K. The second is a broader and more intense peak of about 40 kJ mol^{-1} K^{-1} extending from 700 to 760 K. The presence of the smaller peak within the 350–650 K interval indicates an additional phononic activity not present in the pure oxides, suggesting that the configurational disorder of the multicomponent cation sublattice activates extra vibrational modes in this intermediate-temperature regime. Overall, the heat-capacity behavior of HEO-Tb reveals a non-additive lattice response, where chemical complexity enhances the vibrational density of states and produces a richer phonon spectrum than that of the constituent sesquioxides.

X-ray diffractometry

Crystal structure

Figure 4 summarizes the crystallographic response of the rare-earth sesquioxides and the corresponding high-entropy oxides (HEOs). Panel (a) shows the XRD patterns of the reference Ln_2O_3 (Ln = Dy, Gd, Y, Yb, Lu), all crystallizing in the cubic bixbyite structure (space group $Ia\bar{3}$) after calcination at 800 °C for two

hours. The diffractograms exhibit sharp reflections without peak splitting or secondary phases, confirming long-range cubic symmetry and establishing a robust structural baseline. The systematic shift of peak positions across the lanthanide series reflects the expected lanthanide contraction, and the refined lattice parameters are fully consistent with reported crystallographic data.

Panel (b) displays the XRD pattern of terbium oxide, which cannot be indexed within the bixbyite structure. The diffraction features correspond to triclinic $Tb_{11}O_{20}$ (space group $P\bar{1}$), characterized by a dense set of reflections and pronounced symmetry lowering. This low-symmetry phase arises from the mixed-valence character of terbium (Tb^{3+}/Tb^{4+}) and the associated oxygen non-stoichiometry, which generate locally distorted coordination environments. Among the lanthanides considered here, terbium is the only element capable of stabilizing a mixed-valence state, owing to the electronic accessibility of the Tb^{3+} ($4f^8$) $\leftrightarrow$ Tb^{4+} ($4f^7$) redox couple. As a consequence, terbium forms superstoichiometric oxides such as Tb_4O_7 and $Tb_{11}O_{20}$, whose triclinic metrics contrast sharply with the cubic symmetry of the other sesquioxides. Panel (c) shows the XRD patterns of HEO-Lu and HEO-Tb. Despite the structural incompatibility of triclinic $Tb_{11}O_{20}$ in its single-component form, both HEOs crystallize as single-phase cubic bixbyite structures ($Ia\bar{3}$), with no detectable traces of triclinic or secondary phases. All reflections are well indexed within the cubic symmetry, and no peak splitting is observed. This demonstrates that configurational entropy stabilizes a common average structure, overriding the intrinsic tendency of terbium oxide toward symmetry lowering. In HEO-Tb, the absence of $Tb_{11}O_{20}$ reflections indicates that terbium cations are fully incorporated into the cubic lattice, adopting an average coordination environment compatible with the bixbyite framework. Panel (d) provides an enlarged view of a representative cubic reflection. In the single-component Ln_2O_3 oxides, peak positions vary systematically with the ionic radius of Ln^{3+}, consistent with lattice-parameter changes driven by lanthanide contraction. For the HEOs, the reflections appear at intermediate 2θ positions relative to the parent oxides, in agreement with Vegard-like behavior. The modest peak broadening observed in the HEOs is attributed to microstrain and crystallite-size effects inherent to

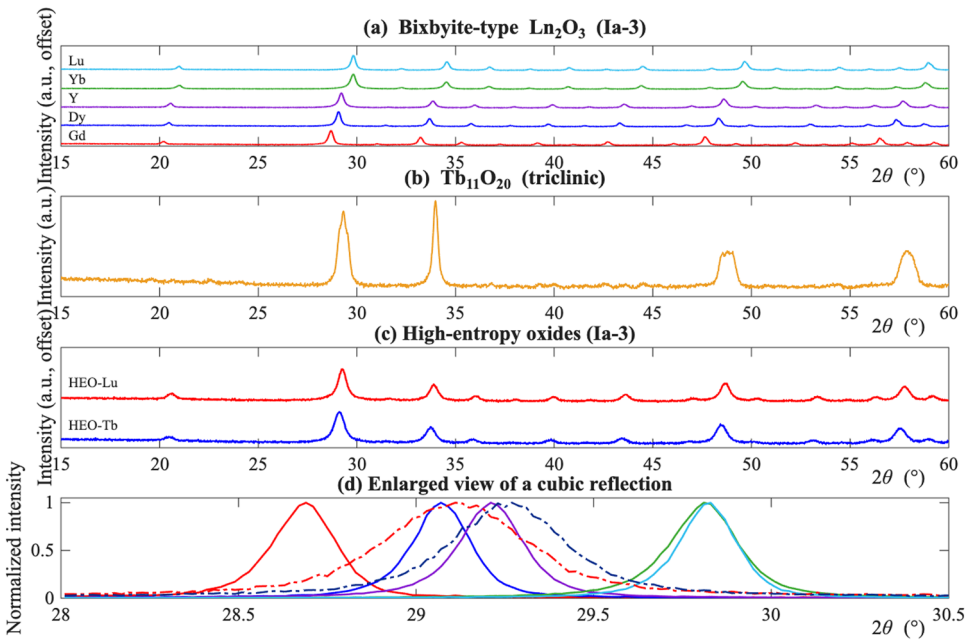


Figure 4 X-ray diffraction (XRD) patterns of rare-earth oxides and high-entropy oxides. **a** Bixbyite-type Ln_2O_3 (Ln = Dy, Gd, Y, Yb, Lu) crystallizing in the cubic $Ia\bar{3}$ space group. **b** Triclinic $Tb_{11}O_{20}$ ($P\bar{1}$) exhibiting additional reflections due to symmetry lowering. **c** High-entropy oxides HEO-Tb and HEO-Lu, both forming a single-phase cubic bixbyite structure ($Ia\bar{3}$). **d** Enlarged view of a representative cubic reflection highlighting peak alignment and limited broadening in the HEOs, indicative of a homogeneous solid solution stabilized by configurational entropy.

multicomponent solid solutions, rather than to structural phase separation.

X-ray photoelectron spectroscopy (XPS)

The Tb core-level signal is relatively weak, and the spectrum reported in Fig. 5 results from the accumulation of eight scans. The main component (#3), centered at 147.7 eV, is fully compatible with trivalent terbium in Tb_2O_3. In the literature, Tb^{3+} is typically observed in the ranges 147.4–147.8 eV [31] and around 147.1 eV [32], whereas Tb^{4+} appears at much higher binding energies, namely 152.1-–155.6 eV [31] and near 155.7 eV [32]. Since no spectral weight is detected in the characteristic Tb^{4+} region, we exclude the presence of Tb^{4+} within the detection limits of our measurement. However, XPS cannot rule out intermediate oxidation states between Tb^{3+} and Tb^{4+}, as such states would only produce subtle shifts within the Tb^{3+} multiplet envelope and remain indistinguishable from coordination- or screening-induced variations. The lower-binding-energy components (#1 and #2), located around 146 eV, are therefore attributed to Tb^{3+} species experiencing different local coordination or final-state screening environments, rather than distinct oxidation states or specific terbium oxide phases such as $Tb_{11}O_{20}$ or Tb_4O_7. As XPS is inherently surface-sensitive, it cannot discriminate between these bulk phases and only indicates that the outermost layers of HEO-Tb are dominated by trivalent terbium.

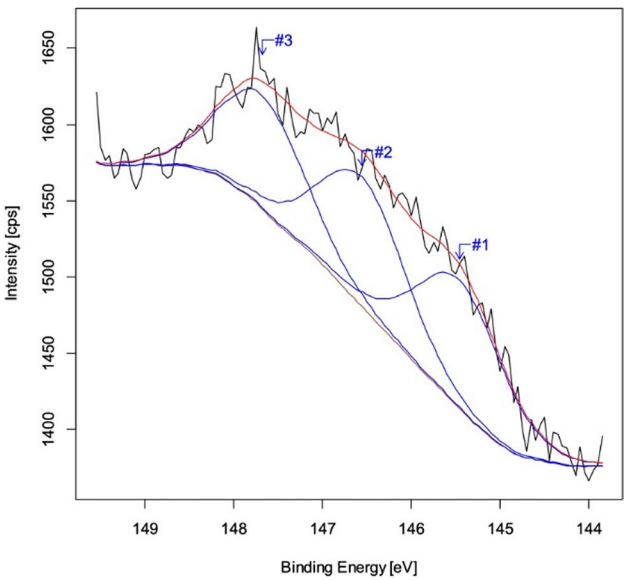


Figure 5 X-ray photoelectron spectroscopy (XPS) analysis of the Tb 3*d* core level for HEO-TbTb. The experimental spectrum (black line) is deconvoluted into the spin-orbit doublet Tb $3d_{5/2}$ and Tb $3d_{3/2}$, each fitted with three components (#1-#3, blue curves) accounting for multiplet splitting and final-state effects typical of trivalent terbium. The resulting envelope (red curve) reproduces the experimental line shape with high fidelity. No intensity is detected in the characteristic Tb^{4+} region (152–156 eV), confirming that terbium remains fully trivalent at the surface of the high-entropy oxide.

Synchrotron total-scattering analysis

To determine whether the structural tendencies of terbium observed in the single-component oxides persist in the multicomponent environment, synchrotron total-scattering measurements were performed on the HEO-Tb composition. This experiment probes both the average and local structure with high real-space resolution, providing a stringent test of whether terbium induces distortions, mixed valence, or symmetry lowering within the high-entropy bixbyite lattice.

Figure 6a shows the high-energy diffraction pattern of HEO-Tb after background subtraction. The reflections are sharp, symmetric, and free of shoulders or extra peaks, demonstrating that HEO-Tb remains single-phase and cubic at the average-structure level. To test specifically for a triclinic Tb-rich contribution in the HEO-Tb, the experimental PDF residuals were compared with the characteristic correlations expected for triclinic $Tb_{11}O_{20}$-type environments [33]. The calculated triclinic structure contains a prominent Tb - Tb correlation near 3.77 Å, followed by a sequence of features at approximately 5.82, 8.62–8.84, 11.78, 12.74 and 13.79 Å. No coherent sequence of residual peaks at these positions was observed following refinement with the cubic bixbyite model [34]. Importantly, no signatures of terbium-rich secondary phases such as $Tb_{11}O_{20}$ or Tb_4O_7 are detected. This confirms that, unlike in the binary oxide where terbium strongly favors low-symmetry polymorphs, the multicomponent environment stabilizes a fully trivalent Tb state and suppresses the structural instabilities typically associated with terbium oxides. The reduced total-scattering structure functions $F(Q)$ reported in Fig. 6b further support this conclusion. Curves processed with different Q_{max} values overlap closely across the entire measured range, with no oscillatory behavior or high-Q artifacts. This stability ensures reliable Fourier transformation and indicates that the extracted

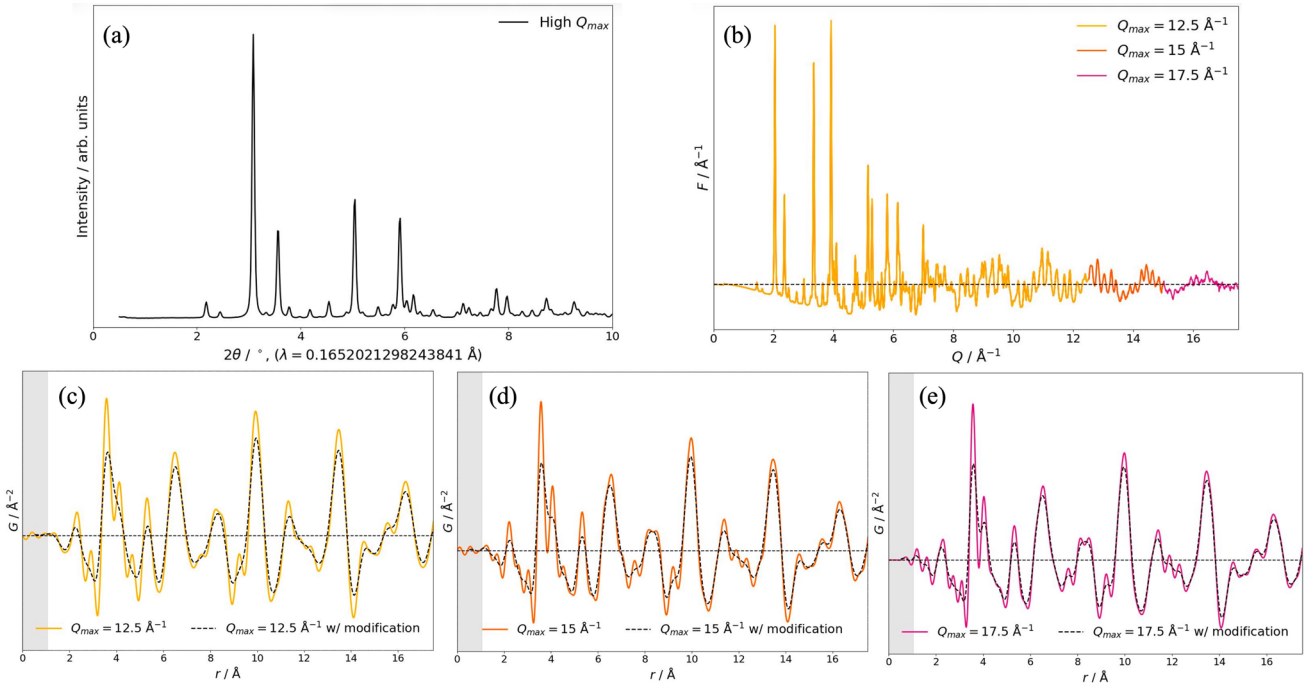


Figure 6 **a** Synchrotron diffraction pattern after background subtraction, showing sharp and symmetric cubic reflections with no evidence of secondary phases such as $Tb_{11}O_{20}$. **b** Reduced total-scattering structure functions $F(Q)$ processed with different Q_{max}, demonstrating stable high-Q behavior and the absence of oscillatory artifacts. **c–e** Pair distribution functions $G(r)$ obtained with Q_{max} = 12.5, 15, and 17.5 Å^{-1}, respectively. All curves display well-defined Ln–O and Ln–Ln correlations consistent with a cubic bixbyite local environment, with no signatures of Tb-rich distortions or short-range ordering.

local-structure information is robust with respect to the choice of Q_{max}. The pair distribution function is obtained through

$$G(r) = \frac{2}{\pi} \int_0^{Q_{max}} Q\,F(Q)\,\sin(Qr)\,dQ \tag{5}$$

highlighting the need for a stable high-Q signal to achieve accurate real-space resolution.

Figure 6c–e displays the resulting pair distribution functions $G(r)$ for Q_{max} = 12.5, 15, and 17.5 Å^{-1}. Across all three values, the first-shell peaks corresponding to Ln–O distances are well defined and consistent with the cubic bixbyite coordination environment. No additional features, shoulders, or peak splittings are observed, demonstrating the absence of local distortions or short-range ordering involving terbium. Increasing Q_{max} improves real-space resolution, but the overall peak shapes and positions remain unchanged, confirming that the local structure is homogeneous and cubic.

The agreement among the three $G(r)$ curves indicates that HEO-Tb exhibits a fully averaged local environment, with no evidence of mixed-valence Tb domains, symmetry-lowered motifs, or nanoscale structural heterogeneity. The absence of local deviations is fully consistent with the smooth thermal response and the lack of calorimetric anomalies, confirming that the multicomponent lattice remains cubic and structurally coherent across all probed length scales. However, the PDF result should not be interpreted as proof of absolute atomic-scale homogeneity. The maximum reliable Q_{max} of 17.5 Å^{-1} corresponds to a nominal real-space resolution of approximately 0.18 Å, while the similar X-ray scattering factors of the constituent heavy rare-earth elements limit the element specificity of the PDF analysis. Very small, highly disordered or low-concentration Tb-rich domains, subtle chemical short-range order and weak local symmetry breaking may therefore remain below the detection limit. Anyway, the absence or attenuation of a collective Tb-related anomaly in the HEO-Tb cannot be attributed uniquely to configurational entropy. Tb occupies only 20% of the cation sublattice, and the probability of forming extended Tb - Tb connectivity is consequently reduced relative to the binary oxide.

Compositional dilution and interruption of Tb - Tb nearest-neighbor networks therefore provide the most direct explanation for the attenuation of a cooperative Tb-rich structural or redox transformation. Configurational entropy may contribute indirectly by favoring retention of the homogeneous multication state and opposing Tb segregation, while local strain and the chemical environment imposed by the other rare-earth cations may modify the Tb^{3+}/Tb^{4+} energetics (Figs. 7, 8, and 9).

Effect of thermal history and prolonged annealing

The cubic bixbyite structure was obtained under all the investigated thermal conditions. Single-phase patterns were recorded after direct calcination of the amorphous precursor at 800 °C for 1 and 2 h and at 1500 ° for 1 h. The same phase was retained after further annealing for 16 h at both 800 and 1500 °C, without detectable additional reflections attributable to Tb-rich, fluorite-like or other secondary crystalline phases. The formation of bixbyite directly from the amorphous precursor at both 800 and 1500 °C, together with its persistence after prolonged annealing at 1500 °C, argues against its interpretation as a transient crystallization product simply frozen during cooling. SEM-EDXS maps collected after 1 and 16 h at 1500 °C showed substantially uniform and co-localized distributions of Dy, Y, Gd, Yb and Tb over the investigated regions. In particular, no micrometer-scale Tb enrichment or depletion was detected after prolonged high-temperature exposure. The combined diffraction and microchemical results therefore demonstrate substantial thermal and compositional robustness of the Tb-containing bixbyite within the investigated processing window. Nevertheless, ex situ XRD and SEM-EDXS do not prove that this phase represents the global equilibrium free-energy minimum. Extremely slow decomposition, nanoscale segregation below the experimental resolution or transformations occurring under different oxygen chemical potentials cannot be excluded.

Optical properties

All samples exhibit absorption edges in the ultraviolet region, consistent with the wide-band-gap character of rare-earth sesquioxides. Band-gap energies were extracted using the Kubelka–Munk formalism and are summarized in Table 1. For the single-component Ln_2O_3 oxides (Ln = Dy, Gd, Y,Yb, Lu), the measured band gaps lie systematically at the lower bound of the literature ranges. This trend reflects band-gap renormalization driven by defect-assisted absorption tails and local structural disorder, consistent with the bixbyite lattice and the weak hybridization between O 2*p* and Ln 4*f* states near the valence-band maximum. Y_2O_3,Gd_2O_3, and Dy_2O_3 exhibit band gaps around 4.8–−4.9 eV, whereas Yb_2O_3 and Lu_2O_3 display slightly reduced gaps (4.6 and 4.4 eV), reflecting the increased lattice compactness and the enhanced sensitivity of the conduction-band edge to local structural perturbations in oxides with filled or nearly filled 4*f* shells. The terbium-containing oxide exhibits a distinct optical response. The band gap of Tb_2O_3 (4.5 eV) is governed by the structural complexity of triclinic $Tb_{11}O_{20}$ and the presence of localized electronic states associated with oxygen non-stoichiometry. Under oxidizing conditions, mixed-valence Tb^{3+}/Tb^{4+} redox fluctuations introduce intragap states that broaden the absorption edge [35]. However, under the nitrogen atmosphere used in this work, TGA and DSC measurements demonstrate that terbium remains fully trivalent, suppressing the formation of Tb^{4+}-bearing phases. Consequently, the optical spectrum of Tb_2O_3 measured here reflects the intrinsic response of trivalent terbium rather than mixed-valence electronic localization. The high-entropy oxides display optical properties that deviate markedly from those of their single-component analogs. Both HEO-Lu and HEO-Tb exhibit band gaps in the 4.8-–4.9 eV range, significantly larger than those of Lu_2O_3 and Tb_2O_3, respectively. These values cannot be rationalized as equimolar averages of the constituent oxides. Instead:

- HEO-Lu exhibits a band gap of 4.9 eV, indicating that configurational disorder suppresses the defect-related absorption tail characteristic of pure Lu_2O_3, yielding a renormalized wide-gap electronic structure.
- HEO-Tb exhibits a band gap of 4.8 eV, demonstrating the complete suppression of mixed-valence intragap states and the restoration of a clean bixbyite-like band edge. Configurational disorder eliminates the electronic localization responsible for gap narrowing in triclinic $Tb_{11}O_{20}$, stabilizing a wide-gap cubic electronic environment.

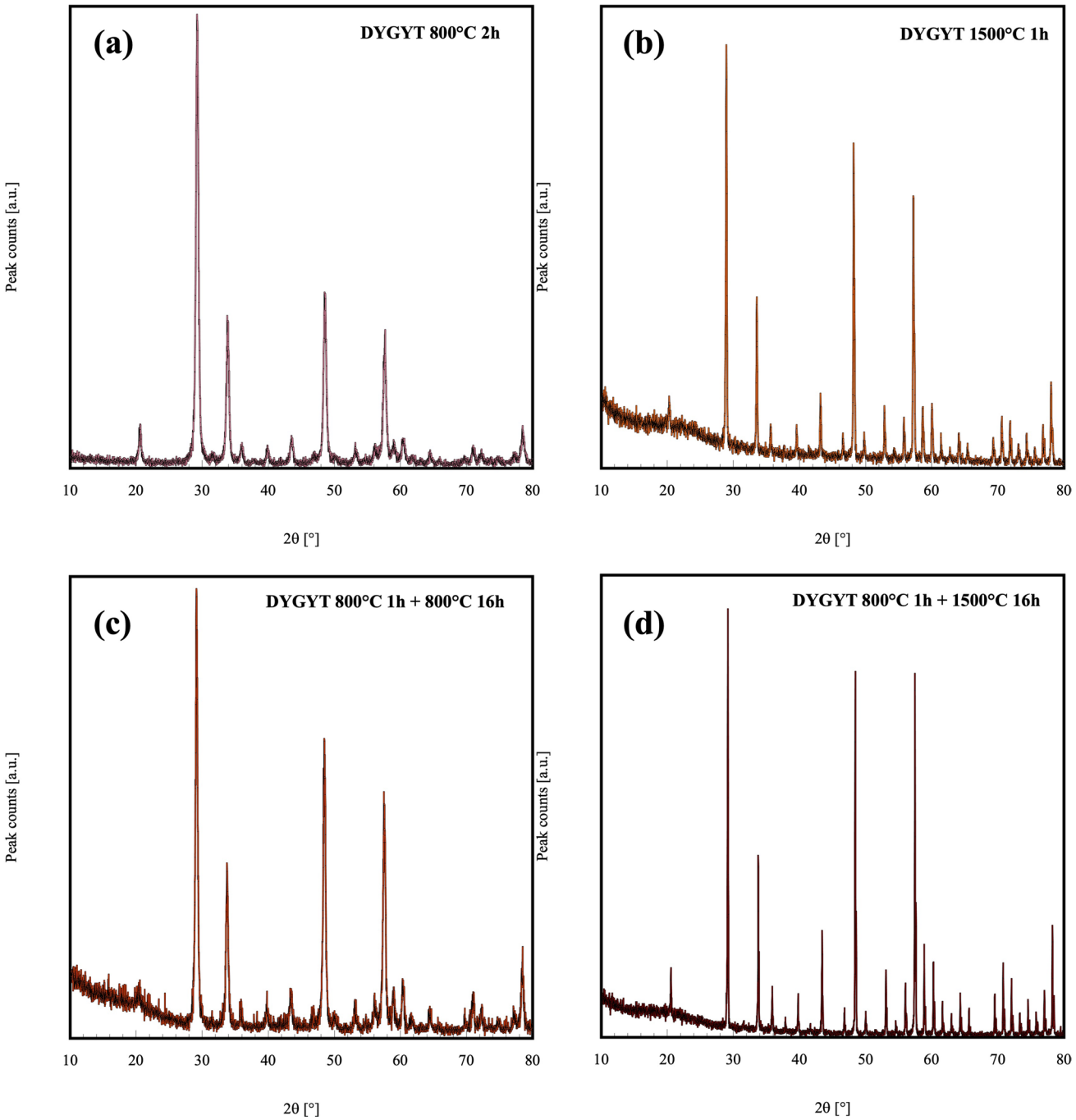


Figure 7 XRD pattern of the calcined HEO-Tb samples: **a** directly from the as-precipitate at 800 °C for 2 h, **b** directly from the as-precipitate at 1500 °C for 1 h, **c** from the already calcined sample at 800 °C 1 h, for extra 16 h at 800 °C, **d** from the already calcined sample at 800°C 1 h, for extra 16 h at 1500 °C.

These observations indicate that configurational disorder in the high-entropy lattice drives a homogenization of the electronic structure [36, 37]. The broad distribution of local coordination environments averages out cation-specific perturbations of the band edges, suppressing the localized states that dominate the optical response of Tb_2O_3. In HEO-Tb, the absence of mixed-valence signatures in the optical spectra is fully consistent with the suppression of redox-driven transitions observed in TGA/DSC and

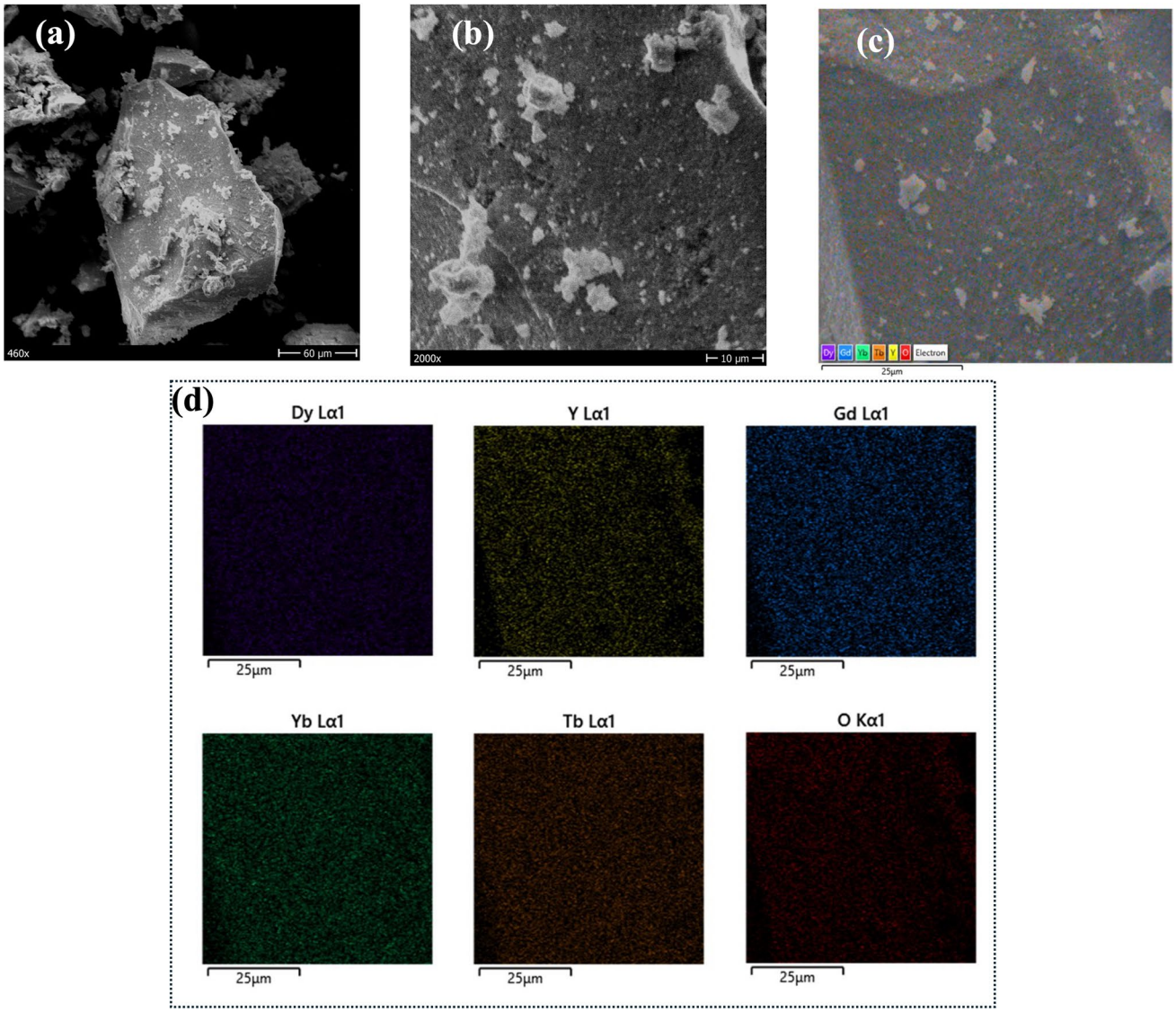


Figure 8 Figure 2: SEM micrographs and EDXS maps for HEO-Tb calcined at 1500 °C for 1h.

with the cubic local structure revealed by synchrotron total scattering. Overall, the optical behavior of the high-entropy oxides mirrors the entropy-driven averaging observed in their thermal and structural properties. The disordered lattice reduces the influence of individual cation chemistry on the band-edge states, yielding a more uniform electronic landscape. This homogenization is particularly evident in the Tb-containing HEO, where the complex electronic structure of terbium oxide is replaced by a smoother, wide-gap bixbyite-like absorption edge. These results demonstrate that configurational entropy not only stabilizes the crystal structure but also renormalizes the electronic degrees of freedom, suppressing localized states and producing band gaps characteristic of an averaged, entropy-stabilized electronic environment.

Conclusions

This work demonstrates that configurational entropy acts as an important mechanism governing the structural, thermodynamic, vibrational, and electronic behavior of multicomponent rare-earth oxides. The single-component Ln_2O_3 sesquioxides (Ln = Gd, Dy, Y, Yb, Lu) provide a stable reference framework, as they crystallize in the cubic bixbyite structure, exhibit

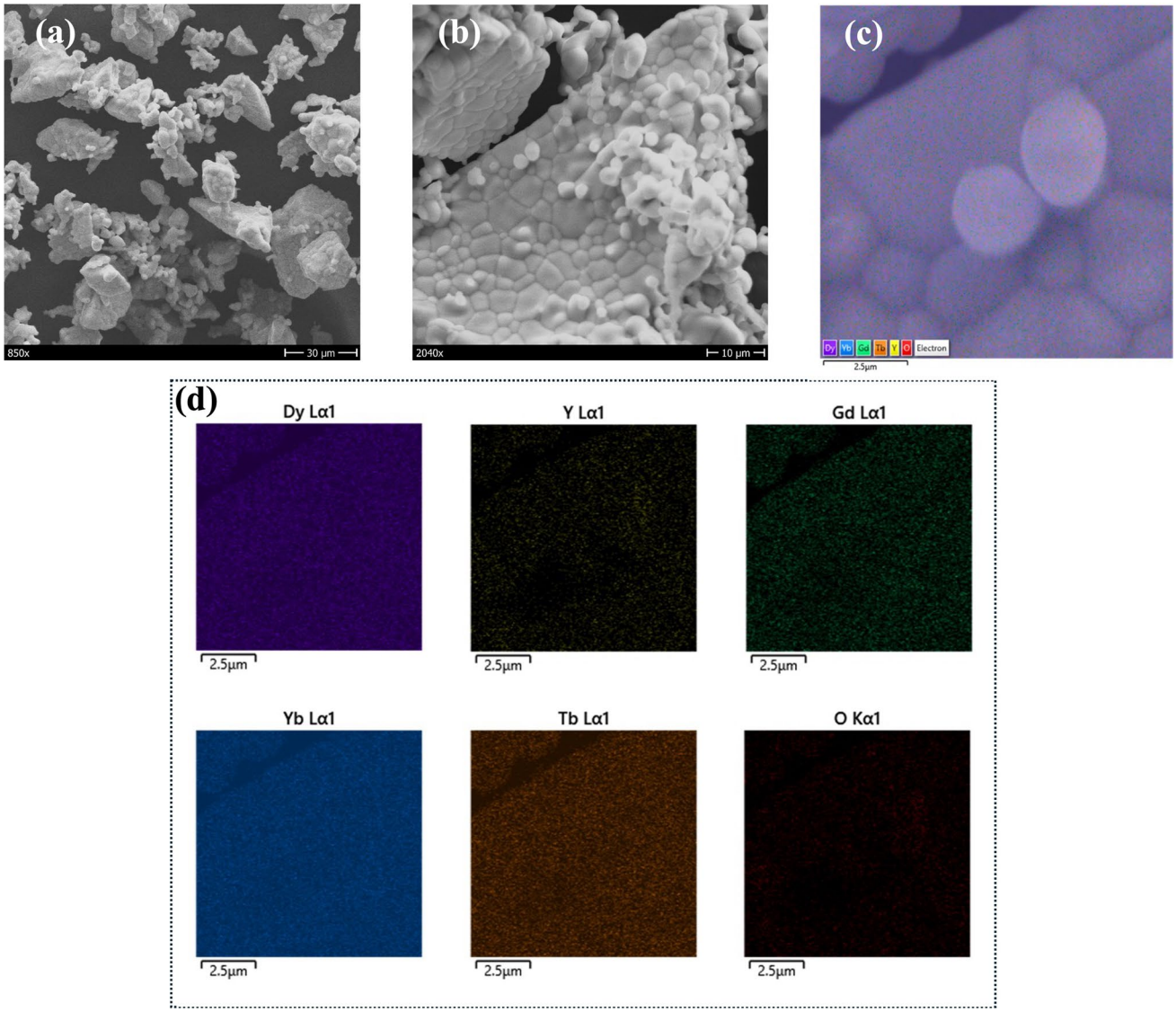


Figure 9 SEM micrographs and EDXS maps for HEO-Tb calcined at 1500 °C for 16h.

Table 1 Measured optical band gaps of single-component oxides and high-entropy oxides, compared with literature values for the corresponding sesquioxides

Oxide	Band gap (eV)	Literature (eV)	References
Dy_2O_3	4.8 ± 0.1	4.8–−5.2	[38, 39]
Gd_2O_3	4.8 ± 0.3	5.2–−5.6	[38, 39]
Y_2O_3	4.9 ± 0.2	5.5–−6.0	[39, 40]
Yb_2O_3	4.6 ± 0.3	4.9–−5.4	[38, 39]
Lu_2O_3	4.4 ± 0.9	5.5–−6.2	[39, 40]
Tb_2O_3	4.5 ± 0.3	4.5–−5.1	[35, 38]
HEO-Tb	4.8 ± 0.5	–	–
HEO-Lu	4.9 ± 0.1	–	–

smooth thermal responses, and display wide-band-gap electronic character. In contrast, terbium oxide behaves fundamentally differently in its binary form. The electronic accessibility of the Tb^{3+} ($4f^8$) ↔ Tb^{4+} ($4f^7$) redox couple enables the formation of superstoichiometric phases such as Tb_4O_7 and $Tb_{11}O_{20}$, characterized by oxygen non-stoichiometry, triclinic symmetry, and pronounced electronic localization. Under the nitrogen atmosphere used in this work for thermal characterization, however, the oxygen chemical potential lies far below the threshold required to stabilize Tb^{4+}-bearing phases. TGA and DSC measurements confirm that terbium remains fully trivalent throughout the explored temperature range, eliminating the

redox-driven structural and electronic instabilities typical of mixed-valence terbium oxides. As a result, Tb_2O_3 exhibits a smooth thermal response and a clean optical band edge, free of intragap states. The tested high-entropy oxides provide a stringent test of how configurational entropy reshapes the behavior of chemically complex constituents. Despite the strong tendency of terbium oxide to crystallize in low-symmetry phases, the HEO-Tb adopts a single-phase cubic bixbyite structure. Laboratory XRD reveals symmetric, unsplit reflections with no traces of triclinic $Tb_{11}O_{20}$, while synchrotron total-scattering measurements confirm that the cubic symmetry persists at the local scale. The pair distribution functions show well-defined Ln - O distances without shoulders or peak splitting, demonstrating that configurational disorder promotes a homogeneous local environment, with no short-range symmetry lowering detected. A key outcome of this work is the demonstration that terbium can be fully incorporated into the high-entropy lattice while retaining its ability to host excess oxygen. In the multicomponent environment, terbium accommodates oxygen without triggering structural distortions. This behavior suggests that the high-entropy lattice provides a chemically flexible environment in which terbium can act as an oxygen-storage site while remaining structurally compatible with the bixbyite framework. Such oxygen-buffering capability is suppressed in the binary oxide but becomes thermodynamically accessible and structurally harmless in the high-entropy solid solution. Calorimetric analysis reveals that both tested high-entropy oxides exhibit positive deviations from ideal mixing in their molar heat capacities, reflecting enhanced low-frequency phonon activity and lattice softening induced by configurational disorder. Rather than accumulating the vibrational contributions of the constituent oxides, the disordered lattice suppresses correlated fluctuations and broadens the phonon spectrum, yielding a homogenized thermodynamic response. Optical measurements further support this interpretation: the band gaps of HEO-Lu and HEO-Tb are significantly widened relative to their single-component analogs, demonstrating that configurational disorder suppresses defect-related absorption tails and eliminates the localized electronic states associated with mixed valence in terbium oxide. Furthermore, the ability of terbium to store oxygen without structural distortions in the high-entropy lattice highlights an additional functional dimension of high entropy materials. These findings underscore the potential of entropy-assisted design as a strategy for engineering oxide materials with enhanced structural robustness, tunable phonon spectra, controlled electronic properties, and chemically flexible oxygen-handling capabilities, even when incorporating intrinsically complex constituents such as terbium. As a final highlighting, the conclusions of this study are restricted to two equimolar five-cation rare-earth oxide compositions prepared by a single wet-chemical route and investigated over a defined range of thermal conditions. Although the persistence of single-phase bixbyite after prolonged annealing and the absence of detectable cation segregation demonstrate substantial thermal and compositional robustness, these observations do not establish that the phases represent universally entropy-stabilized oxides (ESOs), very likely being extremely robust high-entropy oxides (HEOs). Configurational entropy cannot be isolated experimentally from cation-size compatibility, average ionic radius, oxygen stoichiometry, local strain, kinetic effects and processing history.

Acknowledgements

A. de Nigris and L. Ambrosone thank the Consorzio Interuniversitario per lo sviluppo dei Sistemi a Grande Interfase (CSGI-Firenze). The authors sincerely thanks Dr. Giorgio Speranza from Fondazione Bruno Kessler, Via Sommarive 18, 38123 Trento, Italy, for his contribution in the XPS measurement of HEO-Tb sample. The authors acknowledge the European Synchrotron Radiation Facility (ESRF) for provision of synchrotron radiation facilities and Momentum Transfer for facilitating the measurements. Jakub Drnec is thanked for assistance and support in using beamline ID31. The measurement setup was developed with funding from the European Union's Horizon 2020 research and innovation program under the STREAMLINE project (grant agreement ID 870313). Measurements performed as part of the MatScatNet project were supported by OSCARS through the European Commission's Horizon Europe Research and Innovation programme under grant agreement No. 101129751.0.3.

Author contributions

de Nigris A. contributed to writing original draft, Investigation, and formal analysis. Spiridigliozzi L.

contributed to investigation, software, and validation. Dell'Agli G. contributed to writing, review and editing and software. Ambrosone L. contributed to writing original draft, methodology, and conceptualization.

Funding

Open access funding provided by Università degli Studi del Molise within the CRUI-CARE Agreement. The authors received no financial support for the research, authorship, and/or publication of this article.

Data availability

Data will be made available on request.

Code availability

Not applicable.

Declarations

Conflict of interest The authors declare that they have no known conflict of financial interest or personal relationships that could have appeared to influence the work reported in this paper.

Ethical approval Not applicable.

Consent to participate Not applicable.

Open Access This article is licensed under a Creative Commons Attribution 4.0 International License, which permits use, sharing, adaptation, distribution and reproduction in any medium or format, as long as you give appropriate credit to the original author(s) and the source, provide a link to the Creative Commons licence, and indicate if changes were made. The images or other third party material in this article are included in the article's Creative Commons licence, unless indicated otherwise in a credit line to the material. If material is not included in the article's Creative Commons licence and your intended use is not permitted by statutory regulation or exceeds the permitted use, you will need to obtain permission directly from the copyright holder. To view a copy of this licence, visit http://creativecommons.org/licenses/by/4.0/.

References

[1] Zinatloo-Ajabshir S (2022) Advanced Rare Earth-Based Ceramic Nanomaterials. Elsevier, Amsterdam, pp 13–45

[2] Zhi M, Yue S, Zheng L, Su B, Fu J, Sun Q (2024) Recent developments in solid-solid phase change materials for thermal energy storage applications. Journal of Energy Storage 89:111570

[3] Amiri A, Shahbazian-Yassar R (2021) Recent progress of high-entropy materials for energy storage and conversion. Journal of Materials Chemistry A 9(2):782–823

[4] Shan B-F, Yang J, Xiang X, Zhao Z-Y (2025) High-entropy compounds for photo (electro) catalysis: diverse materials and applications. Journal of Materials Chemistry A 13(18):12808–12827

[5] Liu J, Shao G, Liu D, Chen K, Wang K, Ma B, Ren K, Wang Y (2020) Design and synthesis of chemically complex ceramics from the perspective of entropy. Materials Today Advances 8:100114

[6] Anand G, Wynn AP, Handley CM, Freeman CL (2018) Phase stability and distortion in high-entropy oxides. Acta Mater 146:119–125

[7] Olejnik E (2016) Multicomponent equiatomic rare earth oxides. Materials Research Letters https://doi.org/10.1080/21663831.2016.1220433

[8] Smith R (2025) Performance of exchange-correlation approximations to density functional theory for rare-earth oxides. Comput Mater Sci. https://doi.org/10.1016/j.commatsci.2025.113837

[9] Sarkar A, Mannava PK, Velasco L, Das C, Breitung B, Bhattacharya SS, Kruk R, Hahn H (2022) Determining role of individual cations in high entropy oxides: structure and reversible tuning of optical properties. Scripta Mater 207:114273

[10] Li H, Zhou Y, Liang Z, Ning H, Fu X, Xu Z, Qiu T, Xu W, Yao R, Peng J (2021) High-entropy oxides: advanced research on electrical properties. Coatings 11(6):628

[11] Lee JY, Cai W (2024) From fabrication to mechanical properties: exploring high-entropy oxide thin films and coatings for high-temperature applications. Frontiers in Coatings Dyes and Interface Engineering 2:1417527

[12] Pianassola M, Anderson K, Agca C, Benmore CJ, McMurray JW, Neuefeind JC, Melcher C, Zhuravleva M (2023) In situ high-temperature structural analysis of high-entropy rare-earth sesquioxides. Chem Mater 35(3):1116–1124

[13] Wakefield G, Keron H, Dobson P, Hutchison J (1999) Structural and optical properties of terbium oxide nanoparticles. J Phys Chem Solids 60(4):503–508
[14] Johnson L (2025) Lanthanide l-edge spectroscopy of high-entropy oxides: insights into valence and phase stability. Journal of Materials Chemistry A. https://doi.org/10.1039/D5TA03815D
[15] Kumar S et al (2025) Resolving Structural Transitions in Lanthanide High-Entropy Oxides. arXiv preprint. https://doi.org/10.48550/arXiv.2512.03881
[16] Spiridigliozzi L, Monfreda V, Marocco A, Dell Agli G (2025) On the effect of kinetics on the formation of fluorite/bixbyite-structured entropy-stabilized oxides. Ceram Int 51(20):30684–30692
[17] Finger L, Cox D, Jephcoat A (1994) A correction for powder diffraction peak asymmetry due to axial divergence. Applied Crystallography 27(6):892–900
[18] Terban MW, Billinge SJL (2021) Structural analysis of molecular materials using the pair distribution function. Chem Rev 122(1):1208–1272
[19] Egami T, Billinge SJL (2003) Underneath the Bragg Peaks: Structural Analysis of Complex Materials. Pergamon Press, Elsevier, Oxford, England, pp 27–54
[20] Coelho AA (2018) Topas and topas-academic: an optimization program integrating computer algebra and crystallographic objects written in c++. J Appl Crystallogr 51:210–218
[21] Marlton F, Ivashko O, Zimmerman M, Gutowski O, Dippel A-C, Jørgensen MRV (2019) A simple correction for the parallax effect in x-ray pair distribution function measurements. J Appl Crystallogr 52:1072–1076
[22] Peterson PF, Božin ES, Proffen T, Billinge SJL (2003) Improved measures of quality for atomic pair distribution functions. Z Kristallogr 36:53
[23] Billinge SJL, Farrow CL (2013) Towards a robust ad-hoc data correction approach that yields reliable atomic pair distribution functions from powder diffraction data. J Phys: Condens Matter 25:454202
[24] Juhás P, Davis T, Farrow CL, Billinge SJL (2013) Pdfgetx3: A rapid and highly automatable program for processing powder diffraction data into total scattering pair distribution functions. J Appl Crystallogr 46:560–566
[25] Lorch E (1969) Neutron diffraction by germania, silica and radiation-damaged silica glasses. J Phys C: Solid State Phys 2:229–237
[26] Von Dreele R, Eyring L, Bowman A, Yarnell J (1975) Refinement of the crystal structure of pr7o12 by powder neutron diffraction. Structural Science 31(4):971–974
[27] Sugihara T, Lin SH, Eyring L (1981) The kinetics of oxidation of ϕ-phase terbium oxide: $72\,Tb_2O_{3+\delta} + (34-74\delta)\,O_2 \rightarrow Tb_7O_{12}$. J Solid State Chem 40(2):189–196
[28] Neupane CP, Sylvester J, Mudiyanselage DM, Singhapurage HA, Ganikhanov F (2022) Ultrafast phonon decay in complex oxides. Optics 3(4):438–446
[29] Riffe WT, Zare S, Ardrey KD, Champagne VK III, Milich M, Lee K, Jassas M, Makarem S, Opila EJ, Clarke DR (2025) Broadband optical phonon scattering reduces the thermal conductivity of multi-cation oxides. Nat Commun 16(1):3333
[30] Grau Turuelo C, Pinnau S, Breitkopf C (2021) Estimating a stoichiometric solid s gibbs free energy model by means of a constrained evolutionary strategy. Materials 14(2):471
[31] Glätzle M, Janka O, Svitlyk V, Chernyshov D, Bartsch M, Zacharias H, Pöttgen R, Huppertz H (2018) The high-pressure oxide tb3o5 and its non-centrosymmetric low-temperature polymorph-a comprehensive study. Chemistry-A European Journal 24(57):15236–15245
[32] Gupta P, Mahapatra P, Choudhary R (2020) Tbfeo3 ceramic: an exciting colossal dielectric with ferroelectric properties. physica status solidi (b) 257(1):1900236
[33] Baran S, Duraj R, Hoser A, Penc B, Szytuła A (2013) Crystal structure and magnetic properties of tb_11o_20. Acta Phys Pol, A 123(1):98–100
[34] Artini C, Costa GA, Pani M, Lausi A, Plaisier J (2012) Structural characterization of the ceo2/gd2o3 mixed system by synchrotron x-ray diffraction. J Solid State Chem 190:24–28
[35] Yang L, Miklavcic SJ (2004) Revised kubelka-munk theory. i. theory and application. J Opt Soc Am A 21(10):1933–1941
[36] Cox PA (2010) Transition Metal Oxides: an Introduction to Their Electronic Structure and Properties. Oxford University Press, Oxford, pp 157–204
[37] Dorenbos P (2013) Lanthanide 4f-electron binding energies and the nephelauxetic effect in wide band gap compounds. J Lumin 136:122–129
[38] Dorenbos P (2003) The electronic structure of lanthanide sesquioxides. J Lumin 104:239–260
[39] Gillen R, Robertson J (2010) Band structures and optical spectra of lanthanide oxides. Phys Rev B 82:125116
[40] French RH (1990) Electronic band structure of yttrium and lutetium oxides. J Am Ceram Soc 73:477–489

Publisher's Note Springer Nature remains neutral with regard to jurisdictional claims in published maps and institutional affiliations.